



HAL
open science

Continuous wave operation of InAs-based quantum cascade lasers at 20 μ m

Z. Loghmari, M. Bahriz, A. Meguekam, H. Nguyen Van, Roland Teissier, A. Baranov

► **To cite this version:**

Z. Loghmari, M. Bahriz, A. Meguekam, H. Nguyen Van, Roland Teissier, et al.. Continuous wave operation of InAs-based quantum cascade lasers at 20 μ m. Applied Physics Letters, 2019, 115 (15), pp.151101. 10.1063/1.5119242 . hal-02379656

HAL Id: hal-02379656

<https://hal.science/hal-02379656>

Submitted on 25 Nov 2020



HAL is a multi-disciplinary open access archive for the deposit and dissemination of scientific research documents, whether they are published or not. The documents may come from teaching and research institutions in France or abroad, or from public or private research centers.

L'archive ouverte pluridisciplinaire **HAL**, est destinée au dépôt et à la diffusion de documents scientifiques de niveau recherche, publiés ou non, émanant des établissements d'enseignement et de recherche français ou étrangers, des laboratoires publics ou privés.

Continuous wave operation of InAs-based quantum cascade lasers at 20 μm

Cite as: Appl. Phys. Lett. **115**, 151101 (2019); <https://doi.org/10.1063/1.5119242>

Submitted: 10 July 2019 . Accepted: 25 September 2019 . Published Online: 08 October 2019

Z. Loghmari,  M. Bahriz, A. Meguekam, H. Nguyen Van, R. Teissier, and  A. N. Baranov



View Online



Export Citation



CrossMark

ARTICLES YOU MAY BE INTERESTED IN

Hybrid plasmonic metasurfaces

Journal of Applied Physics **126**, 140901 (2019); <https://doi.org/10.1063/1.5116885>

Spintronic GdFe/Pt THz emitters

Applied Physics Letters **115**, 152401 (2019); <https://doi.org/10.1063/1.5120249>

A method for fast and robustly measuring the state of polarization of arbitrary light beams based on Pancharatnam-Berry phase

Journal of Applied Physics **126**, 133105 (2019); <https://doi.org/10.1063/1.5120123>



Your Qubits. Measured.

Meet the next generation of quantum analyzers

- Readout for up to 64 qubits
- Operation at up to 8.5 GHz, mixer-calibration-free
- Signal optimization with minimal latency

Find out more



Continuous wave operation of InAs-based quantum cascade lasers at 20 μm

Cite as: Appl. Phys. Lett. **115**, 151101 (2019); doi: [10.1063/1.5119242](https://doi.org/10.1063/1.5119242)

Submitted: 10 July 2019 · Accepted: 25 September 2019 ·

Published Online: 8 October 2019



View Online



Export Citation



CrossMark

Z. Loghmari, M. Bahriz,^{a)} A. Meguekam, H. Nguyen Van, R. Teissier, and A. N. Baranov

AFFILIATIONS

IES, University of Montpellier, CNRS, F-34000 Montpellier, France

^{a)} Author to whom correspondence should be addressed: michael.bahriz@umontpellier.fr

ABSTRACT

We report low threshold continuous wave (CW) operation of InAs/AlSb quantum cascade lasers emitting around 20 μm . The laser cavity was made of a plasmon-enhanced dielectric waveguide with cladding layers made of n-InAs. The devices exhibited a threshold current density of 1.38 kA/cm² at the maximum temperature of CW operation of 240 K and an output power of 14 mW/facet at T = 80 K. In pulsed mode, the lasers operated up to 380 K with a threshold current density of 1.15 kA/cm² at room temperature.

Published under license by AIP Publishing. <https://doi.org/10.1063/1.5119242>

Quantum cascade lasers (QCLs) have now become the sources of choice for wavelengths beyond 4 μm . Many applications require semiconductor lasers operating in the continuous wave (CW) regime. The first QCLs operating in the CW regime at room temperature (RT) were demonstrated in 2002 at a wavelength of 9.6 μm using the InP-based materials.¹ The threshold current density J_{th} was 5.8 kA/cm² at the maximum temperature operation of 312 K. Achievement of CW operation becomes more challenging with the increasing emission wavelength. The longest wavelength of RT CW operation of InP-based QCLs reported to date is 12.5 μm .² Continuous wave RT operation at 15 μm with a low J_{th} value of 1.3 kA/cm² was demonstrated in InAs-based QCLs.³ Recently, a record long wavelength RT CW operation at 17.7 μm has been achieved in InAs/AlSb QCLs.⁴ Close to the reststrahlen band between 30 and 60 μm , QCL performances are penalized by strong multiphonon and free carrier absorption.⁵ GaAs-based QCLs were demonstrated operating up to 220 K for wavelengths around 15 μm and up to 100 K for wavelengths around 23 μm .⁶ Ohtani *et al.* report InP-based QCLs operating up to 240 K at 24 μm .⁷ Below the reststrahlen band, the longest emission wavelength of 28 μm with a maximum temperature of pulsed operation of 175 K with $J_{\text{th}} = 5.8$ kA/cm² at 10 K was demonstrated in InP-based QCLs.⁸ InAs-based QCLs have already shown their capability of high performance operation at long wavelengths,³ thanks to large optical gain provided by the small electron effective mass in InAs.⁹ The longest wavelength reported for InAs/AlSb QCLs is 25 μm with $T_{\text{max}} = 240$ K in pulsed mode.¹⁰ Using these materials, we demonstrated $T_{\text{max}} = 353$ K in QCLs emitting near 20 μm with a RT threshold current density of 4.4 kA/cm² in pulsed mode.¹¹ However, the threshold

current density was not compatible with the continuous wave regime. In this Letter, we present an advancement of this work. A design improvement allowed us to significantly decrease the threshold current density and thus to reach CW operation at temperatures achievable with Peltier cooling.

The threshold current density must be minimized to reach continuous wave operation. The threshold current density J_{th} is given by the following equation:

$$J_{\text{th}} = J_{\text{tr}} + \frac{\alpha_m + \alpha_w}{g\Gamma} = J_{\text{leak}} + \frac{\alpha_{\text{AR}}}{g} + \frac{\alpha_w}{g\Gamma} - \frac{Ln(R)}{g\Gamma} \frac{1}{L}, \quad (1)$$

where J_{tr} is the transparency current, g is the differential gain coefficient of the active zone, Γ is the optical confinement factor of the fundamental mode of the waveguide, α_{AR} is the absorption in the active region, α_w is the waveguide loss, R is the laser facet reflectivity, and $\alpha_m = -Ln(R)/L$ is the mirror loss.

In this work, we employed a dielectric plasmon-enhanced waveguide that proved to be more efficient for InAs-based QCLs emitting around 20 μm (Ref. 11) than a metal waveguide commonly used in long wavelength QCLs.¹² However, to ensure efficient optical confinement, the thickness of a dielectric waveguide needs to be scaled with the operating wavelength, which is a difficulty for molecular beam epitaxy (MBE) growth and thermal dissipation. In such a waveguide, α_w is mostly due to free carrier absorption in the doped InAs cladding layers. The doping level of the cladding layer can be chosen considering the trade-off between the waveguide loss and optical confinement. In this work, we decreased the doping level of the cladding layers from 3×10^{17} cm⁻³ in our previous work¹¹ to 2×10^{17} cm⁻³, which

provides a complex refractive index $n = 3.053 + 0.00624i$ at a wavelength of $20 \mu\text{m}$. In order to reduce the overlap of the guided optical mode with the absorbing cladding layers and to minimize α_w , the active zone is enclosed between spacer layers made of undoped InAs. The optimal geometry of the QCL waveguide was chosen using the threshold gain as a figure of merit.

The laser threshold is reached when the gain above the transparency current is equal to the total optical losses consisting of the waveguide loss and the mirror loss. The threshold gain G_{th} can be expressed as

$$g(J_{th} - J_{tr}) = G_{th} = \frac{\alpha_m + \alpha_w}{\Gamma}. \quad (2)$$

The mirror loss α_m was calculated for a facet reflectivity $R = 0.29$ and a typical length of the devices $L = 3.6 \text{ mm}$. The complex refractive index of the used materials was calculated using parameters from Refs. 13 and 14 and the Drude model. The loss α_w and confinement factor Γ of the fundamental mode of the waveguide were extracted from modeling using a commercial finite element solver (COMSOL). For the chosen cladding doping level and an emission wavelength of $20 \mu\text{m}$, the threshold gain calculated from Eq. (2) is displayed in Fig. 1 as a function of the thickness of the spacer and cladding layers.

The general conclusion of this simulation is that thicker layers are required to obtain a lower G_{th} . Thin cladding layers lead to a leakage of the optical mode into the metal contact, whereas thin spacers increase the mode overlap with the absorbing claddings. However, too thick spacers (beyond $4 \mu\text{m}$) reduce the optical confinement factor, which will result in increasing threshold gain. For this study, we have chosen a waveguide composed of $4\text{-}\mu\text{m}$ -thick cladding layers and an active region with a total thickness of $7 \mu\text{m}$ separated from the doped layers by $3\text{-}\mu\text{m}$ -thick spacers. This geometry provides a calculated threshold gain $G_{th} = 12.2 \text{ cm}^{-1}$ and $\alpha_w = 4.3 \text{ cm}^{-1}$. The overlap of the fundamental mode with the active region is $\Gamma = 63\%$, thus giving a ratio $\Gamma/\alpha_w = 0.15 \text{ cm}$. For comparison, simulations were performed for a QCL employing a double metal (DM) waveguide and the same active region. The confinement factor of such a structure is $\Gamma = 98\%$, but the waveguide loss $\alpha_w = 17 \text{ cm}^{-1}$ is about four times higher. The

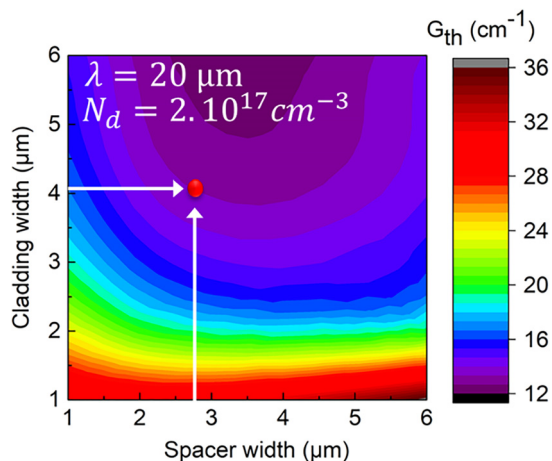


FIG. 1. Threshold gain as a function of the thickness of spacer and cladding layers. The red dot corresponds to the chosen waveguide geometry.

double metal waveguide provides a slightly higher facet reflectivity $R = 0.33$. The threshold gain of the DM QCL is calculated to be $G_{th} = 20.5 \text{ cm}^{-1}$ and $\Gamma/\alpha_w = 0.058 \text{ cm}$, which confirms the advantages of the dielectric waveguide of the chosen configuration.

In this work, we employed a QCL active region similar to that of Ref. 11, presented in Fig. 2(a). It is based on a vertical transition in four coupled quantum wells. The vertical scheme is often used in InAs-based QCLs in order to reduce the impact of interface scattering at InAs/AlSb interfaces with a large conduction band offset of 2.1 eV .¹⁵ The main difference of the new design, shown in Fig. 2(b), is a much lower doping level, reduced from $4 \times 10^{11} \text{ cm}^{-2}$ per period in the reference structure¹⁰ to $9 \times 10^{10} \text{ cm}^{-2}$ (including residual n-type doping of InAs layers of the order of $1 \times 10^{16} \text{ cm}^{-3}$). Another modification is the width of the injector miniband Δ increased from 100 to 120 meV at operating conditions.

The active region contains 70 repetitions of the following layer sequence: **18/119/1.1/96/1.2/88/1.3/85/1.4/84/6/77/5/76/5/72/6/72/10/76/13/75** in Å and starting from the injection barrier, where AlSb layers are in bold and the InAs layers in italics are doped with Si to $3 \times 10^{16} \text{ cm}^{-3}$.

To enhance the available gain, the oscillator strength of the transition is increased from 75 to 89 by increasing the number of wells from 4 to 5 in the laser transition region. The decrease in the doping level is aimed at a reduction of the transparency current J_{tr} [Eq. (1)]. First of all, this modification reduces the leakage current J_{leak} caused by nonresonant electron injection from the injector directly to the lower level of the laser transition.¹⁶ The contribution of J_{leak} is more important in our QCLs with vertical transitions compared with diagonal structures where the laser transition region is separated from the injector by an additional quantum well. The other component of J_{tr} , the resonant optical absorption α_{AR} , is highly dependent on the thermal population of the lower level of the laser transition. It can be expressed as $n_{th} = N_s \exp(-\Delta/kT)$, where N_s is the injector doping level, k is the Boltzmann constant, and T is the electronic temperature.¹⁷ This thermal backfilling is significantly reduced in the new design compared with the previous one because of the increased Δ and, most importantly, the decreased doping level.

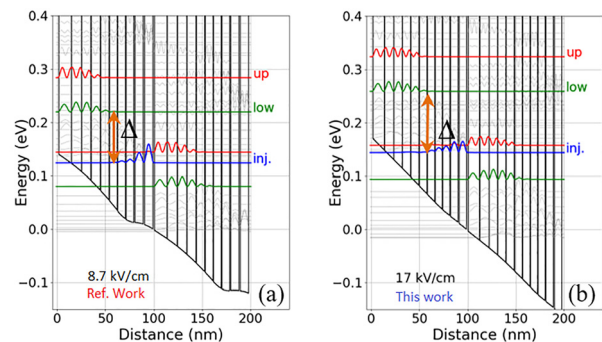


FIG. 2. Conduction band diagram of two periods of the laser active region and moduli squared of the relevant electron wave functions. Δ represents the injector miniband width. (a) Reference design from Ref. 11. (b) Design employed in this work. The smaller band bending is due to lower doping compared with the reference structure.

We calculated the main QCL characteristics using a transport model based on the rate equation method, considering the scattering mechanisms between all subbands of one period of the active zone and the tunneling between subbands of adjacent periods. The total gain (including resonant and nonresonant intersubband absorption) was derived from the populations of the subbands. Figure 3 represents the voltage and the material gain as a function of current density calculated for $T = 280$ K for the reference and the new QCL structures. The maximum current density J_{max} in the new structure is decreased from 5 to 2.4 kA/cm^2 due to the lower doping level. This decrease is smaller than the doping reduction because of the thinner injection barrier, 18 \AA instead of 21 \AA in the previous design. The main result is that the calculated leakage current in the new structure is significantly reduced, as well as the total transparency current, whereas the differential gain of 33 cm/kA is nearly the same in the new structure and the maximum available gain G_{max} of about 50 cm^{-1} is only slightly reduced. Considering the calculated threshold gain values for the chosen waveguide, a threshold current density of about 1.2 kA/cm^2 is expected at $T = 280$ K.

The laser structure was grown on an n-InAs (100) substrate by molecular beam epitaxy (MBE) in a Riber 412 solid source MBE machine equipped with cracker cells for the group-V elements. Growth rates were set to 3 \AA/s for InAs and 1 \AA/s for AlSb. The standard contact photolithography and wet etching were used to fabricate deep mesa ridge lasers. The electrical insulation was ensured by hard-baked positive photoresist. For the electrical contact, a nonalloyed Ti/Au metallization was employed. Devices with cleaved Fabry-Pérot (FP) resonators and uncoated facets were soldered episcide down on copper heat sinks using indium.

The laser emission was collected using an $f/1$ off-axis parabolic mirror and analyzed with a Fourier transform infrared spectrometer (FTIR) Bruker Vertex 70 equipped with a pyroelectric detector. For optical power measurements, the beam was focused on a Melles Griot 13PEM001 power meter with another $f/1$ off-axis parabolic mirror. No correction was made for the light collection efficiency.

Pulsed laser characteristics are shown in Fig. 4. The maximum current density is about 2 kA/cm^2 which is three times lower compared with QCLs from Ref. 11, in close agreement with the theoretical

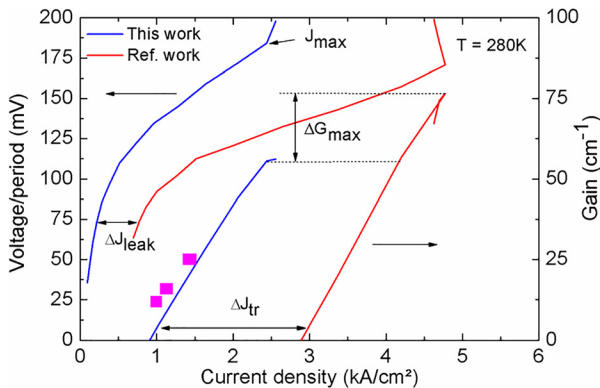


FIG. 3. Voltage and material gain as a function of threshold current density calculated at $T = 280$ K for this work (in blue) and the reference work¹¹ (in red). Pink dots refer to experimental data measured in pulsed mode.

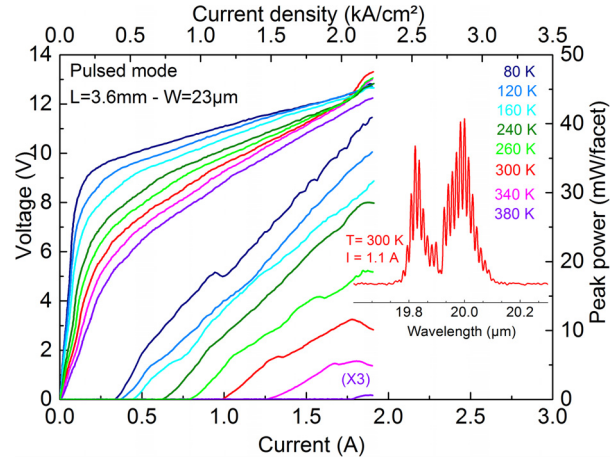


FIG. 4. Voltage-current and light-current characteristics of a 3.6 mm-long and $23 \mu\text{m}$ -wide QCL measured at different temperatures in pulsed mode (333 ns, 12 kHz). Inset: emission spectrum of the laser.

predictions illustrated in Fig. 3. The laser emits around the wavelength of $20 \mu\text{m}$ at RT and operates in pulsed mode up to $T_{max} = 380$ K (Fig. 4). The threshold current density is very low, 0.43 kA/cm^2 at $T = 80$ K and 1.15 kA/cm^2 at RT, which is almost four times better than the previous results (Table I). Unlike in our previous publication (Ref. 11), in this work, we did not notice the effect of the ridge width on the threshold current density of the lasers within the employed $(14\text{--}24)\text{-}\mu\text{m}$ range. We attribute this finding to the improvements in the process of the deposition and subsequent treatment of the insulator layer, which allowed us to significantly reduce the current leakage over the mesa edges that we consider to be the main component of the lateral loss in narrow lasers.

At T_{max} , the threshold current density remains relatively low with $J_{th} = 2.13 \text{ kA/cm}^2$. The characteristic temperature T_0 of the temperature dependence of the threshold current density, estimated close to room temperature, is 205 K which is slightly better than in the reference devices (Fig. 5). It has also to be pointed that this is by far the lowest threshold current density ever obtained for a QCL emitting in this wavelength range.

Figure 6 presents the threshold current density of $20\text{-}\mu\text{m}$ -wide lasers as a function of the reciprocal cavity length. A linear fit of these data following the threshold condition [Eq. (1)] allowed us to determine the differential gain g . The differential gain was found to be 58 and 30 cm/kA at 80 K and RT, respectively, close to the calculated values (Fig. 3). Its temperature dependence is plotted in Fig. 7. This experimental differential gain is lower compared with 100 and

TABLE I. Pulsed performances of the studied lasers in comparison with the reference devices (Ref. 11).

	Ref. work design	This work design
$J_{th} (80 \text{ K}) \text{ kA/cm}^2$	1.38	0.47
$J_{th} (300 \text{ K}) \text{ kA/cm}^2$	4.39	1.15
$J_{th} (T_{max}) \text{ kA/cm}^2$	5.7 (353 K)	2.13 (380 K)

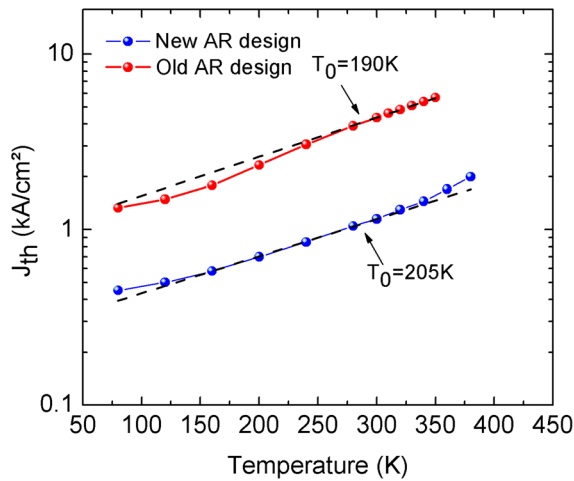


FIG. 5. Temperature dependence of the pulsed threshold current density of the studied laser in comparison with the previous results from Ref. 11. The laser dimensions are 3.6 mm × 23 μm (this work) and 2.92 mm × 50 μm.¹¹

40 cm/kA at 80 and 300 K measured in the reference structure. The new design provides nevertheless much better performances due to the low propagation loss. The total propagation loss, which we can define as $\alpha_{prop} = \Gamma g_{leak} + \Gamma \alpha_{AR} + \alpha_{wg}$, extracted from the data in Fig. 6 is plotted in Fig. 7 as a function of temperature. Compared with the reference lasers, this parameter is significantly reduced, from 70–100 cm⁻¹ to 12–20 cm⁻¹ in the temperature interval of 80–300 K. Figure 6 represents the measurements for lasers with different lengths. The higher mirror loss increases the gain required to achieve threshold in short devices. The threshold gain in lasers of different lengths, extracted using Eq. (2) from the data in Fig. 6 at 280 K, is shown in Fig. 3 (pink squares) as a function of current density. The obtained data are in fair agreement with the calculations for a waveguide loss

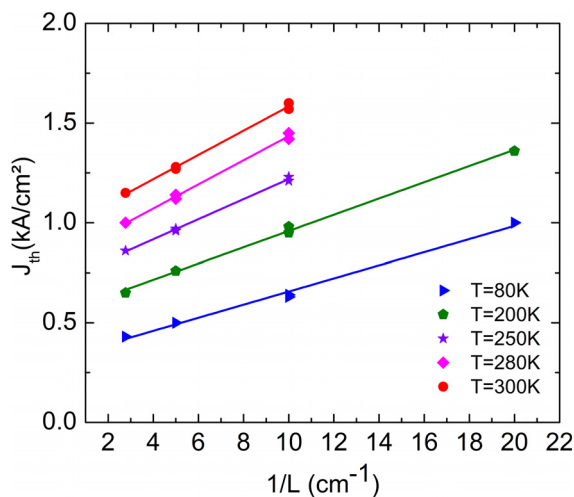


FIG. 6. Threshold current densities as a function of 1/L at different temperatures for 20-μm wide lasers under pulsed mode operation.

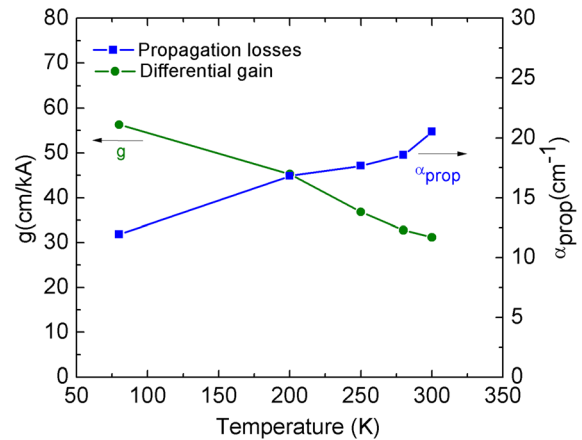


FIG. 7. Differential gain and propagation loss fitted from results of Fig. 6 as a function of temperature.

value = 4.3 cm⁻¹ found from the COMSOL waveguide simulation, thus validating our approach and our active region modeling.

A device with a ridge width of 14 μm was characterized in the continuous wave regime. The voltage-current and light-current characteristics of the laser are shown in Fig. 8 at different temperatures. The threshold current increased from 0.3 A at 80 K up to 0.68 A at 240 K, which is the maximum operation temperature achieved in the CW regime. The output power measured from one facet reached 14 mW at 80 K and 0.3 mW at 240 K.

Figure 9 presents CW emission spectra of this device measured at different temperatures. In the CW regime, the lasers exhibited single frequency emission with a wavelength varying between 20.2 and 20.7 μm depending on temperature. The single frequency behavior was already observed in InAs-based QCLs operating in the CW regime.¹⁸ It was explained by stabilization of the main longitudinal mode when its absorption in the dielectric around laser ridge edges is saturated.

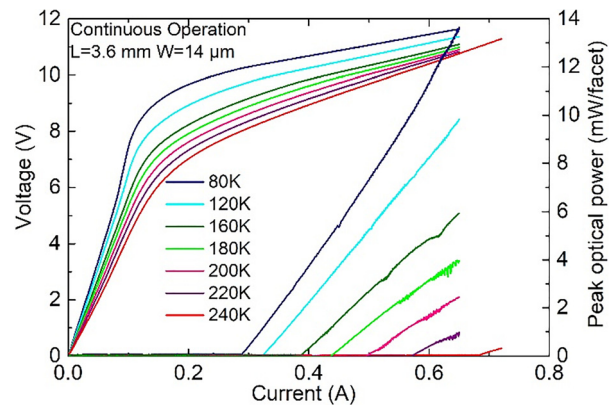


FIG. 8. Voltage-current and light-current characteristics of the laser measured in the continuous wave regime. The laser dimensions are length—3.6 mm and width—14 μm.

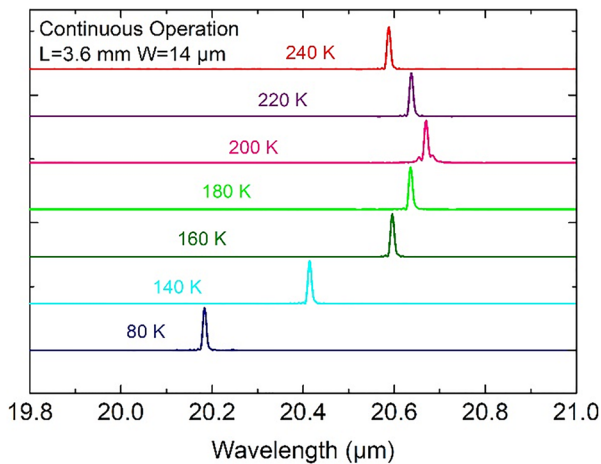


FIG. 9. Temperature evolution of the emission spectra of the laser operating in the CW regime.

In conclusion, we presented in this work InAs/AlSb quantum cascade lasers emitting around $20\ \mu\text{m}$. The lasers operated up to $380\ \text{K}$ in pulsed mode with a RT threshold current density as low as $1.15\ \text{kA}/\text{cm}^2$. The continuous wave regime of operation at temperatures up to $T_{\text{max}} = 240\ \text{K}$ was for semiconductor lasers emitting above $20\ \mu\text{m}$. Electrical and optical characteristics of the lasers are consistent with theoretical predictions, which confirms the validity of the tools and parameters used for the waveguide and active region modeling. The obtained results also confirm the great potential of the InAs/AlSb material system for the development of long-wavelength QCLs.

Part of this work was supported by the French program on “Investments for the Future” [EquipEx EXTRA (ANR-11-EQPX-0016)].

REFERENCES

- M. Beck, D. Hofstetter, T. Aellen, J. Faist, U. Oesterle, M. Ilegems, E. Gini, and H. Melchior, “Continuous wave operation of a mid-infrared semiconductor laser at room temperature,” *Science* **295**(5553), 301–305 (2002).
- Alpes Lasers, see <http://www.alpeslasers.ch/lasers-onstock/sbcw6519.pdf> for “List of CW-RT-DFB-QC Lasers” (last accessed May 8, 2016).
- A. N. Baranov, M. Bahriz, and R. Teissier, “Room temperature continuous wave operation of InAs-based quantum cascade lasers at $15\ \mu\text{m}$,” *Opt. Express* **24**(16), 18799–18806 (2016).
- H. Nguyen-Van, Z. Loghmari, H. Philip, M. Bahriz, A. N. Baranov, and R. Teissier, “Long wavelength ($\lambda > 17\ \mu\text{m}$) distributed feedback quantum cascade lasers operating in a continuous wave at room temperature,” *Photonics* **6**, 31 (2019).
- C. Kittel, “Plasmons, optical phonons, and polarization waves,” *Quantum Theory of Solid* (Wiley, 1987), Chap. 3.
- J. Ulrich, J. Kreuter, W. Schrenk, G. Strasser, and K. Unterrainer, “Long wavelength (15 and $23\ \mu\text{m}$) GaAs/AlGaAs quantum cascade lasers,” *Appl. Phys. Lett.* **80**(20), 3691–3693 (2002).
- K. Ohtani, M. Beck, and J. Faist, “Double metal waveguide InGaAs/AlInAs quantum cascade lasers emitting at $24\ \mu\text{m}$,” *Appl. Phys. Lett.* **105**(12), 121115 (2014).
- K. Ohtani, M. Beck, M. J. Süess, J. Faist, A. M. Andrews, T. Zederbauer, and G. Strasser, “Far-infrared quantum cascade lasers operating in the AlAs phonon reststrahlen band,” *ACS Photonics* **3**(12), 2280–2284 (2016).
- E. Benveniste, A. Vasanelli, A. Delteil, J. Devenson, R. Teissier, A. Baranov, A. M. Baranov, A. M. Andrews, G. Strasser, I. Sagnes, and C. Sirtori, “Influence of the material parameters on quantum cascade devices,” *Appl. Phys. Lett.* **93**(13), 131108 (2008).
- Z. Loghmari, M. Bahriz, A. Meguekam, R. Teissier, and A. N. Baranov, “InAs-based quantum cascade lasers emitting close to $25\ \mu\text{m}$,” *Electron. Lett.* **55**(3), 144–146 (2019).
- M. Bahriz, G. Lollia, A. N. Baranov, and R. Teissier, “High temperature operation of far infrared ($\lambda \approx 20\ \mu\text{m}$) InAs/AlSb quantum cascade lasers with dielectric waveguide,” *Opt. Express* **23**(2), 1523–1528 (2015).
- K. Unterrainer, R. Colombelli, C. Gmachl, F. Capasso, H. Y. Hwang, A. M. Sergent, D. L. Sivco, and A. Y. Cho, “Quantum cascade lasers with double metal-semiconductor waveguide resonators,” *Appl. Phys. Lett.* **80**(17), 3060–3062 (2002).
- M. A. Ordal, L. L. Long, R. J. Bell, S. E. Bell, R. R. Bell, R. W. Alexander, and C. A. Ward, “Optical properties of the metals Al, Co, Cu, Au, Fe, Pb, Ni, Pd, Pt, Ag, Ti, and W in the infrared and far infrared,” *Appl. Opt.* **22**(7), 1099–1119 (1983).
- Y. B. Li, R. A. Stradling, T. Knight, J. R. Birch, R. H. Thomas, C. C. Phillips, and I. T. Ferguson, “Infrared reflection and transmission of undoped and Si-doped InAs grown on GaAs by molecular beam epitaxy,” *Semicond. Sci. Technol.* **8**(1), 101 (1993).
- J. Devenson, R. Teissier, O. Cathabard, and A. N. Baranov, “InAs-based quantum cascade lasers,” *Proc. SPIE* **6909**, 69090U1–69090U9 (2008).
- A. Wittmann, A. Hugi, E. Gini, N. Hoyler, and J. Faist, “Heterogeneous high-performance quantum-cascade laser sources for broad-band tuning,” *IEEE J. Quantum Electron.* **44**, 1083–1088 (2008).
- P. Laffaille, J. C. Moreno, R. Teissier, M. Bahriz, and A. N. Baranov, “High temperature operation of short wavelength InAs-based quantum cascade lasers,” *AIP Adv.* **2**(2), 022119 (2012).
- A. N. Baranov and R. Teissier, “Quantum cascade lasers in the InAs/AlSb material system,” *IEEE J. Sel. Top. Quantum Electron.* **21**(6), 1200612 (2015).